


EXPRESS LETTER

Open Access



# Impact of strong and weak stratospheric polar vortices on geomagnetic semidiurnal solar and lunar tides

Sunil Kumar<sup>1,2</sup>, Tarique A. Siddiqui<sup>3\*</sup> , Claudia Stolle<sup>3</sup>, Nicholas M. Pedatella<sup>4,5</sup> and Duggirala Pallamraju<sup>1</sup>

## Abstract

The impact of strong and weak stratospheric polar vortices on geomagnetic semidiurnal solar and lunar tides is investigated during Northern Hemisphere (NH) winters using ground-based magnetic field observations at the Huancayo (12.05° S, 284.67° E; magnetic latitude: 0.6° S) equatorial observatory. We analyze the periods between December 15 and March 1 for 34 NH winters between 1980 and 2020 and find that the response of semidiurnal solar and lunar tides as seen in geomagnetic field depends on the strength of the stratospheric polar vortex. During weak polar vortex events, geomagnetic semidiurnal solar and lunar tidal amplitudes show an average enhancement by ~25% and ~50%, respectively, which is consistent with the known results during sudden stratospheric warmings. When the stratospheric polar vortex is strong, geomagnetic semidiurnal solar and lunar tidal amplitudes decline on an average by ~15% and ~25%, respectively, during weak polar vortex events. Our results also reveal that the response of the geomagnetic semidiurnal solar tidal variations to strong and weak polar vortex conditions is delayed by approximately 10 days while the response of geomagnetic semidiurnal lunar tidal variations do not show a time delay. These results provide observational evidence that along with weak polar vortices in the Northern Hemisphere, the strong stratospheric polar vortices also have pronounced effects on the equatorial ionosphere.

**Keywords** Strong polar vortex, Weak polar vortex, Stratospheric Sudden Warming, Solar semidiurnal tide, Lunar semidiurnal tide, Equatorial electrojet, Northern Annular Mode, Ionosphere, MLT

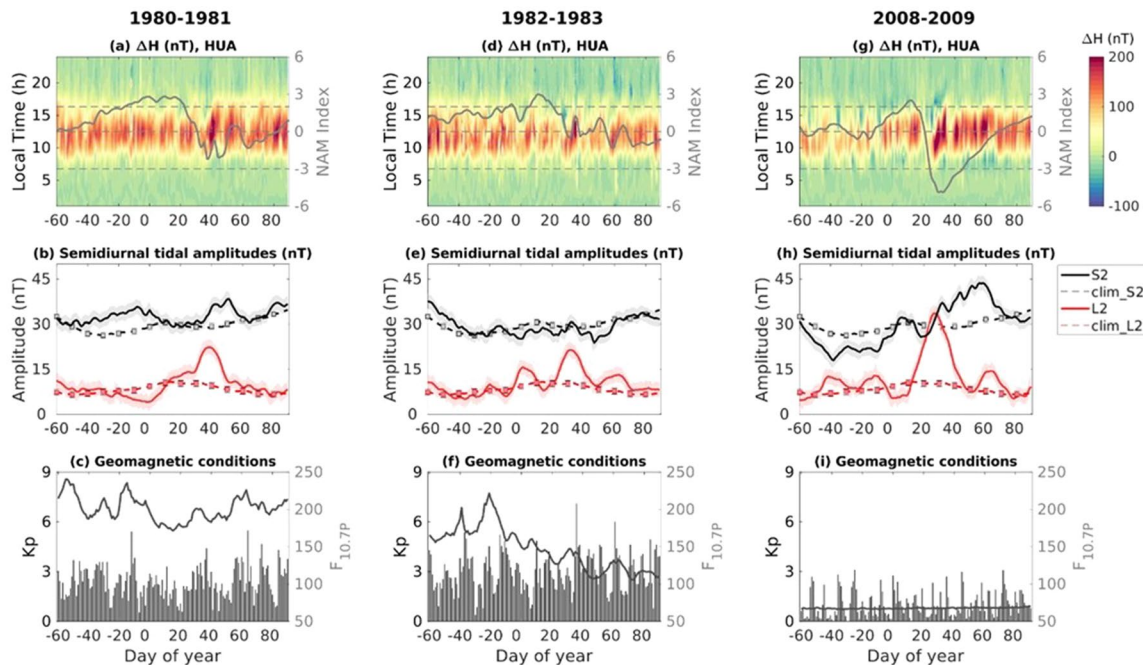
\*Correspondence:

Tarique A. Siddiqui  
siddiqui@iap-kborn.de

Full list of author information is available at the end of the article

## Graphical Abstract

### Plots of geomagnetic semidiurnal solar and lunar tides responding to variability in the stratospheric polar vortex



## Introduction

During winter, the latitudinal variation in insolation causes a large-scale temperature gradient between mid-latitudes and the pole, which results in the formation of the polar vortex in the stratosphere (Baldwin et al. 2021). The stratospheric polar vortex (SPV) is characterized by a band of strong eastward winds that encircle the mid- to high-latitude polar region and span from about 100 hPa to above 1 hPa in altitude. The polar vortex extends well into the mesosphere (Harvey et al. 2018) but the strength of the mesospheric polar vortex is not considered in this study. The SPV experiences large inter-annual variability due to interaction with upward propagating planetary-scale waves that are forced from the troposphere (e.g., Charney and Drazin 1961; Matsuno 1971). These planetary waves (PWs) can propagate vertically and break in the polar stratosphere resulting in the deposition of westward momentum (McIntyre and Palmer 1983), which decelerates the eastward winds of the SPV. Air converges and descends at high-latitudes resulting in warming of the polar stratosphere. Owing to larger topographic and land-sea contrasts, the PWs in the Northern Hemisphere (NH) have larger amplitudes than in the Southern Hemisphere (SH) (e.g., Waugh 2017), which results in the NH SPV being weaker and more prone to distortion than

the SH SPV (e.g., Waugh and Randel 1999). In the NH, a complete breakdown of SPV due to the disruption by PWs is relatively common and happens approximately every 2 years during extreme meteorological events called sudden stratospheric warmings (SSWs) (Charlton and Polvani 2007; Butler et al. 2015). In contrast, SSWs in the SH are rare and have so far only been observed in 2002 and 2019 during the month of September (e.g., Charlton et al. 2005; Yamazaki et al. 2020). During SSWs, a rapid rise in the polar stratospheric temperature by several tens of degrees is often accompanied by a breakdown of the SPV. SSWs are therefore associated with weak polar vortex conditions. Conversely, the development of a strong polar vortex takes place in the absence of strong tropospheric PW activity, which allows for uninterrupted radiative cooling and thereby strengthening of the SPV (e.g., Lawrence et al. 2020). In comparison to SSWs, extended periods of strong polar vortex conditions are relatively rare in the NH mainly because of the short-time scales on which PW forcing can act and rapidly change the state of the SPV (e.g., Lawrence and Manney 2018).

The weak and strong states of SPV play an important role in atmospheric coupling processes and thus have a wide range of impacts in different layers of the atmosphere (e.g., Baldwin et al. 2021; Pedatella and Harvey

2022). In recent decades, the impact of weak SPV conditions on the middle and upper atmospheres in the context of SSWs have been extensively investigated and it is now well-recognized that SSW associated effects can significantly change the dynamics and chemistry of mesosphere, thermosphere and ionosphere (e.g., Goncharenko et al. 2021; Laskar and Pallamraju 2015; Singh and Pallamraju 2015). The SSW-driven variability in the mesosphere and lower thermosphere (MLT) are primarily due to modified gravity wave (GW) forcing that results from the deceleration and reversal of eastward winds of SPV during SSWs (e.g., Holton 1983; Liu and Roble 2002). Additionally, the variability in the ionosphere and thermosphere during SSWs are primarily driven by changes in upward propagating migrating and nonmigrating solar and lunar tides, which result due to a combination of changes in background winds and tidal forcing conditions (e.g., Jin et al. 2012; Forbes and Zhang 2012). Here, tides refer to global-scale oscillations of the atmosphere that have harmonic periods of a solar or a lunar day (Lindzen and Chapman 1969). The upward propagating solar tides are thermally forced and are generated through periodic absorption of solar radiation by water vapour in the troposphere and ozone in the stratosphere whereas the upward propagating lunar tide is primarily forced in the lower atmosphere by the gravitational effects of the moon. For a detailed overview of the impacts of SSWs on the middle and upper atmospheres, the readers may refer to the following reviews by Chau et al., (2012), Baldwin et al., (2021) and Goncharenko et al., (2021). In contrast to the well-studied SSW effects, the impact of strong polar vortex events has only been considerably investigated in the troposphere (e.g., Baldwin and Dunkerton 2001) and is still relatively unknown in the middle and upper atmospheres.

In a recent work by Pedatella and Harvey (2022; hereafter PH22), the impact of strong and weak NH SPV on the MLT has been examined using the Specified Dynamics version of the Whole Atmosphere Community Climate Model with thermosphere-ionosphere eXtension (SD-WACCM-X) simulations. This was the first such study that compared the anomalies in tides, zonal-mean temperature and zonal-mean winds in the MLT during periods of strong and weak NH SPV. From their results, it was found that the response of zonal mean and tidal anomalies during strong SPV are generally opposite in comparison to those that occur during weak SPV periods. The authors further investigated the anomalies in selected atmospheric tides during strong and weak NH SPV time periods and found, in particular, that the migrating semidiurnal solar tide (SW2) shows the most notable change in the MLT with a 25–35% reduction in amplitudes at NH mid-latitudes during strong SPV time

periods. During periods of weak SPV, an even stronger enhancement in SW2 tides was also identified from their results. In comparison, migrating diurnal solar tide (DW1) and non-migrating semidiurnal solar tides (SW1 and SW3) showed smaller changes during strong and weak NH SPV conditions. The work by PH22 did not consider the changes in migrating semidiurnal lunar tide (M2) during periods of either strong or weak SPV as the lunar tidal forcing was not explicitly included in the SD-WACCM-X simulations.

The changes seen in migrating and non-migrating solar tides from the results of PH22 during periods of strong NH SPV could potentially also lead to variability in the ionosphere as it is well-established that the upward propagating tides upon reaching the E-region dynamo heights contribute to the generation of ionospheric currents (e.g., Baker and Martyn 1953). One such current that results due to this ionospheric E-region wind dynamo phenomenon is the equatorial electrojet (EEJ), which is a narrow ribbon of intense current that flows during daytime above the magnetic dip equator. About one-half of the current intensity of the EEJ is driven by the upward-propagating tides (Yamazaki et al. 2014). The EEJ is confined to a latitudinal width of about  $\pm 3$  deg and its high current density is primarily due to the horizontal geometry of the magnetic field lines, which in the presence of large-scale polarisation electric fields enable strongly enhanced (Cowling) conductivity in the ionospheric E-region. The EEJ causes significant magnetic field deflection at ground-based observatories that are located below the magnetic dip equator and therefore magnetic field recordings have been extensively utilized to investigate its various characteristics.

The results of PH22 in the MLT motivate us to compare the ionospheric variability of the semidiurnal solar and lunar tides during periods of strong and weak NH SPV. For this purpose, we use the magnetic field recordings at the Huancayo (HUA, 12.05° S, 284.67° E; magnetic latitude: 0.6° S) observatory to derive the geomagnetic semidiurnal solar and lunar tides. We find that in addition to the known enhancement in geomagnetic semidiurnal solar and lunar tides during periods of SSWs (weak SPV), these tides show a reduction during strong SPV but this decline is not as large as the enhancement during weak SPV conditions. These results demonstrate that in addition to SSWs, periods of strong SPV also lead to considerable impacts in the equatorial ionosphere.

## Data set and analysis methods

### Northern annular mode

The Northern Annular Mode (NAM) accounts for the dominant fraction of extratropical atmospheric circulation variability (e.g., Thompson and Wallace, 1998). In

the troposphere, the NAM characterizes the meridional shifts in the tropical jet streams with its positive phase indicating an increase in the pressure gradient between the mid-latitudes and pole and a poleward displacement of the extratropical jet stream. In the stratosphere, the NAM characterizes the variability in the strength of stratospheric polar vortex (Baldwin and Dunkerton 2001). A positive NAM indicates a stronger than average stratospheric polar vortex and vice versa. In this study, we use the same time-series of NAM index that was used for analysis by PH22. Following the procedure of Gerber and Martineau (2018), the NAM index was calculated based on the average geopotential height anomalies poleward of 65°N at 10 hPa using the National Aeronautics and Space Administration (NASA) Modern-Era Retrospective analysis for Research and Applications version 2 (MERRA-2) reanalysis (e.g., Gelaro et al. 2017). The state of SPV is considered to be strong if the daily NAM at 10 hPa is >2.0 and weak if the daily NAM is <-3.0.

### Geomagnetic semidiurnal solar and lunar tides

Hourly mean values of the horizontal component,  $H$ , of the geomagnetic field observed by the ground-based magnetometer at HUA have been used in this study to estimate the geomagnetic semidiurnal solar and lunar tides for the periods 1980–1991 and 1997–2020. For this purpose, we use a similar technique that has been applied to investigate the geomagnetic lunar tidal modulation in relation to SSWs in earlier studies by Yamazaki et al., (2012) and Siddiqui et al., (2015). The time period of our analysis is similar to the interval that was covered by PH22. The HUA data are available at the website of the World Data Centre (WDC) for Geomagnetism, Edinburgh and have been downloaded for the above-mentioned periods. The data for the years 1991–1996 for HUA remain unavailable.

At the dip equator, the primary sources of the variations in the horizontal component of the geomagnetic field,  $H$ , include contributions from the Earth's main magnetic field ( $H_{MF}$ ), the magnetospheric ring current ( $H_{MP}$ ), and the induced magnetic field due to the large-scale solar quiet (Sq) currents ( $H_{Sq}$ ) and the EEJ ( $H_{EEJ}$ ).

$$H = H_{MF} + H_{MP} + H_{EEJ} + H_{Sq} \quad (1)$$

As Sq and EEJ currents effectively flow only during the daytime and disappear during the night (Malin and Gupta 1977), the quiet night-time values of  $H$  can be used to approximate  $H_{MF}$ . For this purpose, the mean of the night-time values between 23:30 and 02:30 LT for the five monthly International Quiet Days (IQDs) are used. The IQDs are the days where the geomagnetic variations are at a minimum in each month. These night-time values are subtracted from the daily recorded  $H$  data to remove

the effects of the Earth's main magnetic field. During geomagnetically disturbed periods, notable reduction is seen in  $H$  due to the development of a westward ring current in the magnetosphere (e.g., Kamide and Maltsev 2007). To minimize this magnetospheric ring current effect, the  $Dst$  index is used. The contribution of the ring current ( $H_{MP}$ ) is then removed from  $H$  by subtracting the Disturbance Storm Time ( $Dst$ ) index.

$$\Delta H = H - H_{MF} - Dst \quad (2)$$

In equation 2, the daily variation  $\Delta H$  represents the deviation from the quiet-night time levels. The variations in  $\Delta H$  show a dependence on solar activity (Alken and Maus 2007) and in order to consider this dependence we use the solar flux values,  $F_{10.7}$  (in solar flux unit (s.f.u) :  $10^{-22} \text{Wm}^{-2} \text{Hz}^{-1}$ ). We calculate the index  $F_{10.7P}$  using the observed value of  $F_{10.7}$  for each day and its 81-day-centered average,  $F_{10.7A}$ , with the following relation:

$$F_{10.7P} = (F_{10.7} + F_{10.7A})/2 \quad (3)$$

and use it to normalize  $\Delta H$  to a solar flux level of 150 s.f.u with the method described in Park et al., (2012) (see equation 1). We use the index  $F_{10.7P}$  for normalizing  $\Delta H$  since it is known that this index provides a better representation of the solar cycle variations of the solar extreme ultraviolet (EUV) radiation in comparison to  $F_{10.7}$  alone (e.g., Richards et al. 1994).

The geomagnetic solar ( $S$ ) tides control much of the daily variation in  $\Delta H$  and its diurnal ( $S_1$ ) and semidiurnal ( $S_2$ ) components dominate the spectral components of  $\Delta H$ . The geomagnetic solar tides in  $\Delta H$  result due to the contribution of both upward propagating solar tides and in situ generated solar tides in the thermosphere (e.g., Forbes 1982a, 1982b). Additionally, there exist tidal components in  $\Delta H$  that are dependent on the phase of the moon, which are called geomagnetic lunar ( $L$ ) tides. As the atmospheric lunar tides are dominated by its semidiurnal component ( $M_2$ ; 12.421 h), the geomagnetic lunar semidiurnal ( $L_2$ ) component dominates in  $L$ . The amplitude of  $L$  in  $\Delta H$  is typically much smaller than the amplitude of  $S$ , owing to weaker tidal winds. However, on certain so-called 'big-L' days that usually occur during NH winters, the amplitude of  $L$  can become comparable or even larger than that of  $S$  (Bartels and Johnston 1940). Recent studies have pointed out that these 'big-L' days of enhanced lunar amplitudes are associated with the occurrence of SSWs (e.g., Fejer et al. 2010).

In this study, the  $S$  and  $L$  variations of  $\Delta H$  are determined using the Chapman-Miller method that has been summarized in Malin and Chapman (1970). The components of  $S$  and  $L$  can be mathematically expressed as following:



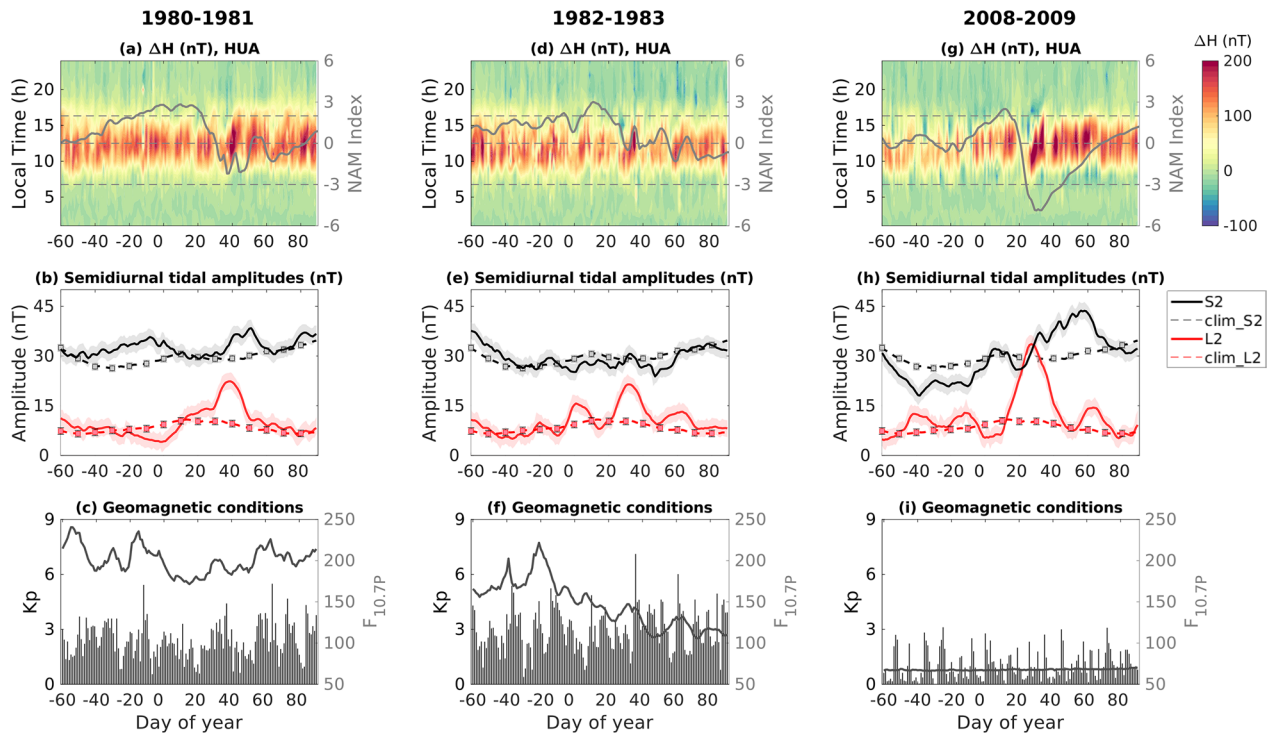


**Fig. 1** Panels **a**, **d** and **g** show the local time variation of  $\Delta H$  from 1st November to 31st March for the winters of years 1980–1981, 1982–1983 and 2008–2009, respectively. The solid gray lines in the top panels represent the NAM values, while dashed gray lines correspond to the NAM value of 2 and -3 associated with the reference values for strong and weak SPV, respectively. In panels **b**, **e** and **h**, the amplitudes of semidiurnal solar (solid black line) tide and its climatology (dashed black line) are shown for the same years as mentioned above. In a similar way, the amplitudes of semidiurnal lunar (solid red line) tide and its climatology (dashed red line) are shown in these figures. The gray and red shadings in these panels indicate the 95% confidence intervals of semidiurnal solar and lunar tides, respectively. The error bars indicate the 95% confidence intervals of the climatological tidal amplitudes. Panels **c**, **f** and **i** show the averaged daily Kp values in black bars and daily  $F_{10.7P}$  levels in solid gray lines

$$S_n = s_n \sin\left(\frac{2\pi}{24}nt + \sigma_n\right) \quad (4)$$

$$L_n = l_n \sin\left(\frac{2\pi}{24}nt - \frac{2\pi}{24}(2\nu) + \lambda_n\right) \quad (5)$$

Here,  $S_n$  and  $L_n$  denote the  $n$ th component of  $S$  and  $L$ , respectively, with corresponding  $s_n$  and  $l_n$  amplitudes. The phases  $\sigma_n$  and  $\lambda_n$  denote the phase angle of the  $n$ th component of  $S$  and  $L$ , respectively. The lunar age in hours is denoted by  $\nu$  and the solar local time in hours is denoted by  $t$ . The  $S$  and  $L$  variations are simultaneously determined by fitting their four respective Fourier coefficients to  $\Delta H$  over a 21-day moving window through an ordinary least-squares (OLS) approach by using equations 4 and 5. The 21-day moving window has been chosen because it allows the separation of solar and lunar semidiurnal tides without generating any major artifacts and has been utilized in similar studies by Chau et al., (2015) and Conte et al., (2017).

Based on the common OLS approach, we employ the classical Gauss-Markov assumptions to estimate the standard errors (SE) of regression coefficients by taking the square root of the diagonal elements of the variance-covariance matrix of the OLS estimator (e.g., Greene 2018; see Chapter 4). Further, the  $s_n$  and  $l_n$  amplitudes are functions of OLS regression coefficients and error propagation formula (e.g., Taylor 1982; Montgomery, 2012; see Chapter 3) is applied to compute the standard errors of tidal amplitudes ( $SE_{\text{tidal}}$ ). The 95% confidence interval of the estimated  $s_n$  and  $l_n$  amplitudes are then constructed using  $SE_{\text{tidal}}$  estimates (see Additional file 1 for complete mathematical derivations). The climatological amplitudes of  $s_n$  and  $l_n$  are obtained by computing the mean of the amplitudes over the 34 analyzed winter periods and its associated standard error ( $SE_{\text{clim}}$ ) is estimated by  $SE_{\text{tidal}}/\sqrt{34}$ , which is then used to construct its 95% confidence interval. It is important to note that the amplitudes of  $S$  and  $L$  that are determined using this method include contributions from migrating and non-migrating semidiurnal solar and lunar tides, respectively.

For a more complete description of the efficacy of this method, the readers are referred to Siddiqui et al., (2018).

## Results

Between 1980 and 2020, there are 24 winters with strong SPV, 12 winters with weak SPV and 4 winters with both strong and weak SPV (see the complete list of dates in the supplemental data of PH22). In Fig. 1, we present the  $S_2$  and  $L_2$  variations in  $\Delta H$  during individual NH winters with both a strong and weak SPV. We select the winters in 1980–1981, 1982–1983 and 2008–2009 for this purpose. These time periods were also analyzed by PH22 (see their Fig. 3). In Figure 1a, the daily  $\Delta H$  values that have been normalized to 150 s.f.u are presented between November 01, 1980 and March 31, 1981. In this figure, the daily diurnal variation of  $\Delta H$  with a maxima during the local noon time can be easily identified. The variations in  $\Delta H$  show a day-to-day variability that are almost entirely confined to daytime hours and these variations are caused by eastward-directed EEJ currents. In Fig. 1a, negative deflections in  $\Delta H$  can also be seen during morning and evening hours, which are related to westward flow of current at these times and are referred to as counter-electrojets (e.g., Yamazaki and Maute 2017). The day-to-day variability of the NAM index is shown in bold gray line in this figure, the values of which are shown in the right y-axis. The dashed gray lines correspond to the NAM value of 2 and  $-3$  associated with the reference values for strong and weak SPV, respectively. The amplitudes of  $S_2$  (black line) and  $L_2$  (red line) tides that are estimated from  $\Delta H$  are presented along with their error estimates in Fig. 1b. The gray and red shadings indicate the 95% confidence intervals of  $S_2$  and  $L_2$  tidal amplitudes, respectively. The dashed black and red lines denote the climatological  $S_2$  and  $L_2$  tidal amplitudes, respectively, with the error bars indicating the 95% confidence intervals of these mean tidal amplitudes. In Fig. 1c, the bar plot presents the daily averaged Kp levels (black bars) and the gray lines correspond to the daily  $F_{10.7P}$  levels during this time interval, the values of which are shown on the right y-axis. From Fig. 1c, we note that this time period was marked by high  $F_{10.7P}$  levels and was also geomagnetically active on days  $-12$  and  $64$  as the averaged daily Kp values remained high. As we account for variability due to geomagnetic activity and solar flux levels in  $\Delta H$  and use a 21-day window for the estimation of tidal amplitudes, we think that any abrupt influence of geomagnetic effects on tides would be smoothed out. As it can be seen in Fig. 1a, the period between mid-December (day  $-15$ ) and late January (day  $23$ ) was characterized by strong SPV conditions as the NAM index remained above 2 during this time. In response to strong SPV conditions,  $S_2$  amplitudes in Fig. 1b decline from  $\sim 36$  nT on day  $-8$  to below

its climatological levels to  $\sim 30$  nT by day 8 and remain at these levels until day 35. A more discernible decline is seen in  $L_2$  with its amplitude showing a reduction from  $\sim 7$  nT on day  $-30$ , which is close to its climatological levels, to  $\sim 4$  nT by day 0. Compared to the slightly lagged response of  $S_2$  to strong SPV conditions, the decline in  $L_2$  amplitudes begin soon after the initial NAM increase from day  $-35$  onward. After day 21, the SPV conditions begin to weaken and NAM starts to decline sharply and eventually reaches  $-2$  by day 37. It remains around this value until mid-February before recovering and rising to 0 in the beginning of March. During this weakening of SPV, a semidiurnal structure with its peak shifting to later local times on succeeding days is seen in  $\Delta H$  appears around day 40 in Fig. 1a, which is associated with  $L_2$  enhancement during SSWs (e.g., Chau et al. 2009; Fejer et al. 2010). Corresponding to this weakened state of SPV, we notice an enhancement in  $S_2$  amplitudes in Fig. 1b as it rises above its climatological levels to  $\sim 36$  nT by day 42 and peaks at  $\sim 39$  nT on day 52. The response of  $L_2$  to weakening SPV is slightly earlier than  $S_2$  and its peak enhancement is seen on day 40 with an amplitude of  $\sim 22$  nT, which is almost two times its climatological levels. As the SPV begins to recover in early March and NAM values increase from their minima,  $S_2$  and  $L_2$  amplitudes decline sharply. The  $L_2$  amplitudes return back to their climatological levels by day 60 but  $S_2$  amplitudes decline below their climatological levels for a few days in early March and gradually begin to return towards this level by the end of March. For this winter, the results of PH22 showed a decline in MLT SW2 amplitudes with a minima centered around day 10 and an enhancement with a maxima centered around day 40. We find that our observation of  $S_2$  in  $\Delta H$  is generally consistent with their findings for this event.

Similar to Fig. 1a, the daily normalized  $\Delta H$  values are presented between November 01, 1982 and March 31, 1983 in Fig. 1d. From the NAM index, it can be seen that strong SPV conditions existed between late December and mid-January for this winter. The SPV weakens first in late January and early February and then again towards the end of February and from mid-March onward. However, it can be seen that based on the NAM index, the extent of weakening of the SPV is slightly reduced in comparison to the 1980–1981 winter. Fig. 1e shows that  $S_2$  amplitudes respond to strong SPV conditions with a decline from  $\sim 30$  nT on day  $-15$  to below their climatological levels by day  $-8$  and reach their minima of  $\sim 25$  nT by day 2. The  $S_2$  amplitudes show a small enhancement in response to declining NAM, which happens around day 0 to record a maxima of  $\sim 28$  nT by day 8. As the NAM values rise again and reach a peak value of  $\sim 3$  on day 11,  $S_2$  amplitudes respond with a decline and reach their

minima of  $\sim 26$  nT by day 21. With a decline in NAM values in late January to levels below 0,  $S_2$  amplitudes show an enhancement and rise above their climatological levels to  $\sim 31$  nT on day 32 before falling back when NAM values increase after this day. Another enhancement in  $S_2$  amplitudes happen towards the end of February when NAM values decline and SPV weakens, which result in  $S_2$  amplitudes reaching above their climatological levels to  $\sim 33$  nT after day 60.

Compared to  $S_2$ , the response of  $L_2$  to the variability of NAM index is more easily recognizable for this winter in Fig. 1e as the minima and maxima in  $L_2$  amplitudes are seen to occur concurrently with increasing and decreasing NAM values, respectively. With a local minima in NAM values around day  $-20$ , an enhancement can be seen in  $L_2$  with its amplitude rising just above its climatological levels to  $\sim 10$  nT. Thereafter, as NAM values increase and relatively stronger SPV conditions exist until day  $-5$ ,  $L_2$  amplitudes decline below their climatological levels to  $\sim 6$  nT. Another local minima in NAM ensues around day 0 and  $L_2$  amplitudes enhance to a local maxima of  $\sim 15$  nT on day 1. As NAM rises above 2 between day 0 and 20,  $L_2$  amplitudes fall below their climatological amplitudes under this strong SPV conditions. Once NAM begins its sharp decline in late January,  $L_2$  amplitudes rise to a maxima of  $\sim 22$  nT on day 31. Associated with this  $L_2$  tidal enhancement, the local time shifting semidiurnal structure in  $\Delta H$  again appears between days 30 and 40 in Fig. 1d. In association with declining NAM, the appearance of afternoon depression in  $\Delta H$  around 15 LT on day 30 can be noticed in Fig. 1d. These depressions are caused by westward counter-electrojet currents that have been reported to be associated with weak SPV conditions (e.g., Fejer et al. 2010). In Fig. 1e, a decline is seen in  $L_2$  amplitudes again as they fall back close to

their climatological levels by day 50 when NAM values increase above 0 after day 46 and peak around day 50. Another enhancement in  $L_2$  is also seen when NAM values decline below 0 around day 60. We note from Fig. 1f that this time period was marked by moderate-to-high  $F_{10.7P}$  levels and was also geomagnetically active especially on day 61 as the averaged daily Kp values reached above 6 on this day.

The daily normalized  $\Delta H$  values are presented between November 01, 2008 and March 31, 2009 in Fig. 1g. From Fig. 1i, we note that this time period was marked by low  $F_{10.7P}$  levels and was also geomagnetically quiet as the averaged daily Kp values remained low. In Fig. 1g, the NAM values remain around 0 in November and mid-December before gradually rising to levels above 2 between late December and mid-January. Higher NAM values correspond to strong SPV conditions during these times. In late January, the NAM values decline sharply to levels below  $-3$  and remain there until mid-February before gradually rising and returning to 0 by mid-March. The period between late January and mid-February correspond to weak SPV conditions, which resulted in the strong 2009 SSW event. Corresponding to strong SPV conditions,  $L_2$  amplitudes in Fig. 1h decline from  $\sim 13$  nT in late December to reach below their climatological levels to  $\sim 5$  nT in mid-January. When SPV conditions become weak in late January,  $L_2$  amplitudes increase to more than 3 times their climatological levels and reach  $\sim 33$  nT by day 28. With the increase in  $L_2$  amplitudes, strong depressions in  $\Delta H$  associated with counter-electrojets is seen around day 26 between 12 and 15 LT in Fig. 1g. Additionally, the development of a multi-day semidiurnal pattern with enhancement of  $\Delta H$  in morning hours and weakening in the afternoon hours that shifts in time on succeeding days can be seen between days 27 and 35 in this figure. This feature in  $\Delta H$  is characteristic of enhanced lunar effects during SSWs and it has also been observed in equatorial F region vertical plasma drifts (e.g., Chau et al. 2009). With the subsequent recovery of the SPV in February,  $L_2$  amplitudes decline to their climatological levels. As seen earlier for the 1980–1981 and 1982–1983 winters,  $S_2$  amplitudes in Fig. 1h also show a slightly delayed response to both strong and weak SPV conditions during the 2008–2009 winter. With strengthening SPV,  $S_2$  amplitudes decline from  $\sim 31$  nT in early January to reach below their climatological levels to  $\sim 26$  nT around day 20. With the weakening of the SPV between late January and mid-February and thereafter its subsequent recovery,  $S_2$  amplitudes gradually increase past their climatological levels by day 24 and eventually reach up to  $\sim 42$  nT on day 50. As the SPV recovers by early March,  $S_2$  amplitudes begin to decline back to their climatological levels.

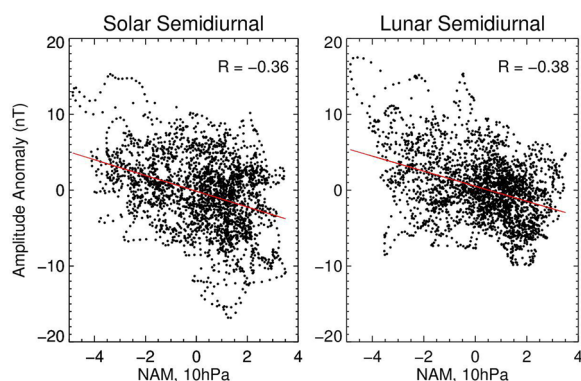


**Fig. 2** Scatter plot between the anomalies in  $S_2$  and  $L_2$  geomagnetic tides versus the Northern Annular Mode (NAM) at 10 hPa. Results are restricted to the period of 15 December to 1 March for all the available data between 1980 and 2020. The  $S_2$  and  $L_2$  tidal anomalies are plotted against NAM with a lag of 10 and 0 days, respectively



## Discussion

From the above results, it can be clearly inferred that geomagnetic semidiurnal solar and lunar tides typically decline in response to strong SPV conditions but with a slightly weaker sensitivity when compared to its enhancement during weak SPV conditions. Thus,  $S_2$  and  $L_2$  tidal amplitudes seem to be anti-correlated to the NAM index especially during strong and weak SPV conditions as larger semidiurnal tidal amplitudes are seen during weak state of SPV and vice-versa. In order to further quantify the relationship between geomagnetic semidiurnal tides and the states of SPV, we plot the  $S_2$  and  $L_2$  tidal anomalies against the NAM at 10 hPa for all available data between December 15 and March 1 for the years 1980–2020 in Fig. 2. Contrary to  $L_2$  tides,  $S_2$  tides generally respond with a time lag to the state of the SPV. While the enhancement and reduction of  $L_2$  amplitudes generally coincide with the fall and rise of NAM index, the  $S_2$  amplitudes do not show enhancement or reduction immediately but with a time lag of several days. To account for this lag, we calculated a median response time of  $S_2$  tides to SPV based on a cross-correlation analysis between  $S_2$  tidal amplitudes and NAM by using discrete lag interval of 0–20 days for each of the winters during the years of 1980–2020 and found it to be around 10 days. Thus, the  $S_2$  and  $L_2$  tidal anomalies are plotted between December 15 and March 1 against NAM with a lag of 10 and 0 days, respectively. The results show that there is a clear linear relationship between  $S_2$  and  $L_2$  tides throughout the different range of states of the SPV. The linear correlation coefficient for  $S_2$  is  $-0.36$  and for  $L_2$  is  $-0.38$ , indicating that  $\sim 15\%$  of the variability in  $S_2$  and  $L_2$  tides during NH winter can be explained by the state of the SPV. Based on this plot, the average enhancement in geomagnetic solar and lunar tidal amplitudes during weak SPV ( $\text{NAM} < -3.0$ ) comes to be  $\sim 25\%$  and  $\sim 50\%$ , respectively. During strong SPV ( $\text{NAM} > 2.0$ ), the geomagnetic solar and lunar tidal amplitudes decline on an average by  $\sim 15\%$  and  $\sim 25\%$ , respectively. It is also important to note that these correlation coefficient values may be longitude dependent and in case if a similar analysis is performed with magnetic-field recordings at a different equatorial station, the results may differ because longitudinal variability of geomagnetic tidal amplitudes during weak SPV conditions have been found in earlier studies (e.g., Siddiqui et al. 2017).

Although our results are based on observations and not on controlled simulations, they compare well with those of PH22 despite focusing on the effects in the ionosphere rather than on the neutral atmosphere. However, we find that the absolute value of linear correlation coefficient between  $S_2$  and NAM is lower and almost half of their reported value for SW2 and NAM. There could be

various reasons for this difference between the responses of  $S_2$  and SW2 tides to NAM. For example,  $S_2$  tides in  $\Delta H$  comprise of different migrating and non-migrating semidiurnal components that have the following main sources: (1) in situ thermal forcing in the thermosphere, and (2) upward-propagating tides that are generated in the lower atmosphere. Since it is not possible to separate the migrating and non-migrating semidiurnal components from single-station observations, the contributions from non-migrating semidiurnal tides are also included in our calculation of  $S_2$  amplitudes. The contributions from non-migrating semidiurnal tides can certainly be non-negligible during SSWs as it has been reported that they can be generated by nonlinear interaction between tides and PWs (e.g., Pedatella and Forbes 2010) and possibly by longitudinal changes in stratospheric ozone distributions (Goncharenko et al. 2012). Additionally, the contributions of in situ generated thermospheric semidiurnal tides, though small (e.g., Forbes and Garrett 1979), are also included in our calculated  $S_2$  amplitudes. Also, it was found by PH22 that the relationship between non-migrating semidiurnal tides (SW1 & SW3) and NAM (see their Additional file 1) is considerably weaker in comparison to SW2. Based on these factors, we presume that the contributions of non-migrating semidiurnal tides and in situ generated semidiurnal tides in  $S_2$  amplitudes may be a reason for the lower correlation coefficient seen between  $S_2$  and NAM in our results in comparison to the results of PH22.

From our results, it was also observed that  $L_2$  tidal variations respond with almost no time lag to the strong and weak states of SPV while  $S_2$  tidal variations responded with a median time lag of around 10 days. It is plausible that the difference in the timing of  $L_2$  and  $S_2$  tidal responses could be due to the mechanisms that drive these tidal variations and further analysis and more research is certainly needed to understand the role of these different processes.

## Conclusions

In this study, we have used the horizontal magnetic field recordings from the Huancayo equatorial observatory to study the variations of geomagnetic semidiurnal solar and lunar tides during periods of strong and weak SPV. Based on the analysis of 34 NH winters between 1980 and 2020, we find that the response of the geomagnetic semidiurnal solar and lunar tides is dependent on the state of the NH SPV. These tides typically show an average enhancement ( $\sim 25\%$  for  $S_2$ ,  $\sim 50\%$  for  $L_2$ ) during times of weak SPV and an average reduction ( $\sim 15\%$  for  $S_2$ ,  $\sim 25\%$  for  $L_2$ ) during times of strong SPV. The decline in tides, however, occurs with a weaker sensitivity during strong



SPV conditions when compared to its enhancement during weak SPV conditions. Our results also reveal that the geomagnetic semidiurnal solar tidal response to strong and weak SPV conditions is delayed by approximately 10 days while the response of geomagnetic semidiurnal lunar tide is almost immediate without any time lag. This suggests that there are different sources of semidiurnal solar and lunar tidal variations that are driving these tidal changes during strong and weak SPV conditions. Further, these results confirm the simulation results of PH22 and provide observational evidence that in addition to weak NH polar vortices, strong NH polar vortices also have a pronounced short-term effect on the semidiurnal solar and lunar tides in the ionosphere.

#### Abbreviations

Dst	Disturbance storm time
DW1	Migrating solar diurnal tide
EEJ	Equatorial electrojet
GFZ	German Research Centre for Geosciences
GW	Gravity wave
HUA	Huancayo
IQD	International quiet day
L2	Geomagnetic semidiurnal lunar tides
M2	Migrating lunar semidiurnal tide
MERRA	Modern era retrospective analysis for research and applications
MLT	Mesosphere lower thermosphere
NAM	Northern annular mode
NH	Northern hemisphere
PW	Planetary wave
S2	Geomagnetic semidiurnal solar tides
SD	Specified dynamics
SH	Southern hemisphere
SPV	Stratospheric polar vortex
SSW	Sudden stratospheric warming
SW1	Nonmigrating solar semidiurnal westward wave-1
SW2	Migrating solar semidiurnal tide
SW3	Migrating solar semidiurnal westward wave-3
Sq	Solar quiet
WACCM-X	Whole atmosphere community climate model with thermosphere and ionosphere extension
WDC	World data centre

#### Supplementary Information

The online version contains supplementary material available at <https://doi.org/10.1186/s40623-023-01810-x>.

**Additional file 1.** Error analysis of tides obtained by least-squares fitting.

#### Acknowledgements

The work at PRL is supported by the Department of Space, Government of India. SK acknowledges support from Leibniz Institute of Atmospheric Physics, Kühlungsborn, Germany during his visit under the SCOSTEP visiting scholar program. This material is based upon work supported by the National Center for Atmospheric Research, which is a major facility sponsored by the U.S. National Science Foundation under Cooperative Agreement 1852977.

#### Author contributions

All the authors contributed to the design, implementation of the result, and writing the manuscript. All authors read and approved the final manuscript.

#### Funding

SK obtain the financial support from Leibniz-IAP, Kühlungsborn, Germany and SCOSTEP under the SCOSTEP visiting scholar program.

#### Availability of data and materials

The results presented in this paper rely on the data collected at Huancayo that have been downloaded using the website of WDC, Edinburgh (<https://wdc.bgs.ac.uk/catalog/master.html>). We thank the INTERMAGNET for promoting high standards of magnetic observatory practice and the Instituto Geofísico del Perú for supporting geomagnetic observatory operations at Huancayo. We are very thankful to WDC for Geomagnetism, Kyoto, for making available the *Dst* indices, which are available at <https://wdc.kugi.kyoto-u.ac.jp/>. The data for *F10.7* and *Kp* were obtained from the GSFC/SPDF OMNIWeb interface at <http://omniweb.gsfc.nasa.gov>. The MERRA-2 data used for calculation of NAM is available via <https://gmao.gsfc.nasa.gov/reanalysis/MERRA-2/>. The International Quiet Days have been downloaded from the website of GFZ Potsdam via the following link <https://www.gfz-potsdam.de/sektion/geomagnetismus/daten-produkte-dienste/geomagnetischer-kp-index>.

#### Declarations

##### Competing interests

The authors declare that they have no competing interests.

##### Author details

<sup>1</sup>Physical Research Laboratory, Space and Atmospheric Sciences Division, Ahmedabad, India. <sup>2</sup>Indian Institute of Technology, Gandhinagar, India. <sup>3</sup>Leibniz Institute of Atmospheric Physics at the University of Rostock, Kühlungsborn, Germany. <sup>4</sup>High Altitude Observatory, National Center for Atmospheric Research, Boulder, CO, USA. <sup>5</sup>COSMIC Program Office, University Corporation for Atmospheric Research, Boulder, CO, USA.

Received: 20 January 2023 Accepted: 21 March 2023

Published online: 10 April 2023

#### References

- Alken P, Maus S (2007) Spatio-temporal characterization of the equatorial electrojet from CHAMP, Ørsted, and SAC-C satellite magnetic measurements. *J Geophys Res Space* 112:A09305. <https://doi.org/10.1029/2007JA012524>
- Baker W, Martyn DF (1953) Electric currents in the ionosphere—the conductivity. *Philos Tr Soc Lond S-A* 246:281–294
- Baldwin MP, Dunkerton TJ (2001) Stratospheric harbingers of anomalous weather regimes. *Science* 294:581–584. <https://doi.org/10.1126/science.1063315>
- Baldwin MP, Ayarzagüena B, Birner T, Butchart N, Butler AH, Charlton-Perez AJ et al (2021) Sudden stratospheric warmings. *Rev Geophys* 59:e2020RG000708. <https://doi.org/10.1029/2020RG000708>
- Bartels J, Johnston H (1940) Geomagnetic tides in horizontal intensity at Huancayo. *Terr Magn Atmos Electr* 45:269–308. <https://doi.org/10.1029/TE045i003p00269>
- Butler AH, Seidel DJ, Hardiman SC, Butchart N, Birner T, Match A (2015) Defining sudden stratospheric warmings. *Bull Am Meteorol Soc* 96(11):1913–1928. <https://doi.org/10.1175/BAMS-D-13-00173.1>
- Charlton AJ, Polvani LM (2007) A new look at stratospheric sudden warmings. Part I: Climatology and modeling benchmarks. *J Clim* 20(3):449–469. <https://doi.org/10.1175/JCLI3996.1>
- Charlton AJ, O'Neill A, Lahoz WA, Berrisford P (2005) The splitting of the stratospheric polar vortex in the Southern Hemisphere, September 2002: dynamical evolution. *J Atmos Sci* 62:590–602. <https://doi.org/10.1175/JAS-3318.1>
- Charney JG, Drazin PG (1961) Propagation of planetary-scale disturbances from the lower into the upper atmosphere. *J Geophys Res* 66(1):83–109. <https://doi.org/10.1029/JZ066i001p00083>
- Chau JL, Fejer BG, Goncharenko LP (2009) Quiet variability of equatorial E × B drifts during a sudden stratospheric warming event. *Geophys Res Lett* 36:L05101. <https://doi.org/10.1029/2008GL036785>

- Chau JL, Goncharenko LP, Fejer BG, Liu H-L (2012) Equatorial and low latitude ionospheric effects during sudden stratospheric warming events. *Space Sci Rev* 168:385–417. <https://doi.org/10.1007/s11214-011-9797-5>
- Chau JL, Hoffmann P, Pedatella NM, Matthias V, Stober G (2015) Uppermesospheric lunar tides over middle and high latitudes during sudden stratospheric warming events. *J Geophys Res Space* 120:3084–3096. <https://doi.org/10.1002/2015JA020998>
- Conte JF, Chau JL, Stober G, Pedatella N, Maute A, Hoffmann P, Janches D, Fritts D, Murphy DJ (2017) Climatology of semidiurnal lunar and solar tides at middle and high latitudes: Interhemispheric comparison. *J Geophys Res Space* 122:7750–7760. <https://doi.org/10.1002/2017JA024396>
- Fejer BG, Olson ME, Chau JL, Stolle C, Lühr H, Goncharenko LP, Nagatsuma T (2010) Lunar-dependent equatorial ionospheric electrodynamic effects during sudden stratospheric warmings. *J Geophys Res* 115:A00G03. <https://doi.org/10.1029/2010JA015273>
- Forbes JM (1982a) Atmospheric tides, 1, model description and results for the solar diurnal component. *J Geophys Res* 87:5222–5240
- Forbes JM (1982b) Atmospheric tides, 2, the solar and lunar semidiurnal component. *J Geophys Res* 87:5222–5240
- Forbes JM, Garrett HB (1979) Theoretical studies of atmospheric tides. *Rev Geophys* 17(8):1951–1981. <https://doi.org/10.1029/RG017I008p01951>
- Forbes JM, Zhang X (2012) Lunar tide amplification during the January 2009 stratosphere warming event: Observations and theory. *J Geophys Res* 117:A12312. <https://doi.org/10.1029/2012JA017963>
- Gelaro R, McCarty W, Suárez MJ, Todling R, Molod A, Takacs L, Randles CA, Darmenov A, Bosilovich MG, Reichle R, Wargan K, Coy L, Cullather R, Draper C, Akella S, Buchard V, Conaty A, da Silva AM, Gu W, Kim G, Koster R, Lucchesi R, Merkova D, Nielsen JE, Partyka G, Pawson S, Putman W, Rienecker M, Schubert SD, Sienkiewicz M, Zhao B (2017) The modern-era retrospective analysis for research and applications, Version 2 (MERRA-2). *J Clim* 30(14):5419–5454. <https://doi.org/10.1175/JCLI-D-16-0758.1>
- Gerber EP, Martineau P (2018) Quantifying the variability of the annular modes: Reanalysis uncertainty vs. sampling uncertainty. *Atmospheric Chem Phys* 18(23):17099–17117. <https://doi.org/10.5194/acp-18-17099-2018>
- Goncharenko LP, Coster AJ, Plumb RA, Domeisen DIV (2012) The potential role of stratospheric ozone in the stratosphere-ionosphere coupling during stratospheric warmings. *Geophys Res Lett* 39:L08101. <https://doi.org/10.1029/2012GL051261>
- Goncharenko LP, Harvey VL, Liu H, Pedatella NM (2021) Sudden stratospheric warming impacts on the ionosphere–thermosphere system. In: Huang C, Lu G, Zhang Y, Paxton LJ (eds) *Ionosphere dynamics and applications*. American Geophysical Union, Washington, DC, pp 369–400
- Greene W (2018) *Econometric analysis*, 8th edn. Pearson Education Limited, London
- Harvey VL, Randall CE, Goncharenko LP, Becker E, France JA (2018) On the upward extension of the polar vortices into the mesosphere. *J Geophys Res Atmos*. <https://doi.org/10.1029/2018JD028815>
- Holton JR (1983) The influence of gravity wave breaking on the general circulation of the middle atmosphere. *J Atmos Sci* 40:2497–2507. [https://doi.org/10.1175/1520-0469\(1983\)040%3C2497:TIOGWB%3E2.0.CO;2](https://doi.org/10.1175/1520-0469(1983)040%3C2497:TIOGWB%3E2.0.CO;2)
- Jin H, Miyoshi Y, Pancheva D, Mukhtarov P, Fujiwara H, Shinagawa H (2012) Response of migrating tides to the stratospheric sudden warming in 2009 and their effects on the ionosphere studied by a whole atmosphere-ionosphere model GAIA with COSMIC and TIMED/SABER observations. *J Geophys Res* 117:A10323. <https://doi.org/10.1029/2012JA017650>
- Kamide Y, Maltsev YP (2007) Geomagnetic storms. In: Kamide Y, Chian A (eds) *Handbook of the Solar-Terrestrial Environment*. Springer, Berlin, pp 355–374
- Laskar FI, Pallamraju D (2015) Does sudden stratospheric warming induce meridional circulation in the mesosphere thermosphere system? *J Geophys Res Space Phys* 119:10133–10143. <https://doi.org/10.1002/2014JA020086>
- Lawrence ZD, Manney GL (2018) Characterizing stratospheric polar vortex variability with computer vision techniques. *J Geophys Res Atmospheres* 123:1510–1535. <https://doi.org/10.1002/2017JD027556>
- Lawrence ZD, Perlwitz J, Butler AH, Manney GL, Newman PA, Lee SH, Nash ER (2020) The remarkably strong arctic stratospheric polar vortex of winter 2020: Links to record-breaking arctic oscillation and ozone loss. *J Geophys Res Atmospheres* 125(22):2020033271. <https://doi.org/10.1029/2020JD033271>
- Lindzen RS, Chapman S (1969) Atmospheric tides. *Space Sci Rev* 10(1):3–188
- Liu H-L, Roble RG (2002) A study of a self-generated stratospheric sudden warming and its mesospheric-lower thermospheric impacts using the coupled TIME-GCM/CCM3. *J Geophys Res Atmos* 107:4695. <https://doi.org/10.1029/2001JD001533>
- Malin SRC, Chapman S (1970) The determination of lunar daily geophysical variations by the Chapman-Miller method. *Geophys J Int* 19:15–35
- Malin SRC, Gupta JC (1977) The Sq current system during the international geophysical year. *Geophys J R Astron Soc* 49:515–529
- Matsuno T (1971) A dynamical model of the stratospheric sudden warming. *J Atmos Sci* 28(8):1479–1494. [https://doi.org/10.1175/15200469\(1971\)028%3C1479:ADMOTS%3E2.0.CO;2](https://doi.org/10.1175/15200469(1971)028%3C1479:ADMOTS%3E2.0.CO;2)
- McIntyre M, Palmer T (1983) Breaking planetary waves in the stratosphere. *Nature* 305:593–600. <https://doi.org/10.1038/305593a0>
- Montgomery DC, Peck EA, Vining GG (2012) *Introduction to linear regression analysis*. John Wiley & Sons, Hoboken
- Park J, Lühr H, Kunze M, Fejer BG, Min KW (2012) Effect of sudden stratospheric warming on lunar tidal modulation of the equatorial electrojet. *J Geophys Res Space* 117:A03306. <https://doi.org/10.1029/2011JA017351>
- Pedatella NM, Forbes JM (2010) Evidence for stratosphere sudden warming-ionosphere coupling due to vertically propagating tides. *Geophys Res Lett* 37:L11104. <https://doi.org/10.1029/2010GL043560>
- Pedatella NM, Harvey VL (2022) Impact of strong and weak stratospheric polar vortices on the mesosphere and lower thermosphere. *Geophys Res Lett* 49:e2022GL098877. <https://doi.org/10.1029/2022GL098877>
- Richards PG, Fennelly JA, Torr DG (1994) EUVAC: A solar EUV flux model for aeronomic calculations. *J Geophys Res* 99:8981–8992. <https://doi.org/10.1029/94JA00518>
- Siddiqui TA, Stolle C, Lühr H, Matzka J (2015) On the relationship between weakening of the northern polar vortex and the lunar tidal amplification in the equatorial electrojet. *J Geophys Res Space Phys* 120:10006–10019. <https://doi.org/10.1002/2015JA021683>
- Siddiqui TA, Stolle C, Lühr H (2017) Longitude-dependent lunar tidal modulation of the equatorial electrojet during stratospheric sudden warmings. *J Geophys Res Space Phys* 122:3760–3776. <https://doi.org/10.1002/2016JL023609>
- Siddiqui TA, Maute A, Pedatella N, Yamazaki Y, Lühr H, Stolle C (2018) On the variability of the semidiurnal solar and lunar tides of the equatorial electrojet during sudden stratospheric warmings. *Ann Geophys* 36:1545–1562. <https://doi.org/10.5194/angeo-36-1545-2018>
- Singh RP, Pallamraju D (2015) On the latitudinal distribution of mesospheric temperatures during sudden stratospheric warming events. *J Geophys Res Space Phys*. <https://doi.org/10.1002/2014JA020355>
- Taylor JR (1982) *An introduction to error analysis*. University Science Books, Sausalito, p 270
- Thompson DWJ, Wallace JM (1998) The arctic oscillation signature in the wintertime geopotential height and temperature fields. *Geophys Res Lett* 25:1297–1300. <https://doi.org/10.1029/98GL00950>
- Waugh DW, Randel WJ (1999) Climatology of arctic and Antarctic polar vortices using elliptical diagnostics. *J Atmos Sci* 56(11):1594–1613. [https://doi.org/10.1175/1520-0469\(1999\)056%3C1594:COAAP%3E2.0.CO;2](https://doi.org/10.1175/1520-0469(1999)056%3C1594:COAAP%3E2.0.CO;2)
- Waugh DW, Sobel AH, Polvani LM (2017) What is the polar vortex and how does it influence weather? *Bull Am Meteor Soc* 98(1):37–44. <https://doi.org/10.1175/BAMS-D-15-00212.1>
- Yamazaki Y, Maute A (2017) Sq and EEJ—a review on the daily variation of the geomagnetic field caused by ionospheric dynamo currents. *Space Sci Rev* 206:299–405. <https://doi.org/10.1007/s11214-016-0282-z>
- Yamazaki Y, Richmond A, Yumoto K (2012) Stratospheric warmings and the geomagnetic lunar tide: 1958–2007. *J Geophys Res Space* 117:A04301. <https://doi.org/10.1029/2012JA017514>
- Yamazaki Y, Richmond AD, Maute A, Wu Q, Ortland DA, Yoshikawa A, Adimula IA, Rabi B, Kunitake M, Tsugawa T (2014) Ground magnetic effects of the equatorial electrojet simulated by the TIE-GCM driven by TIMED satellite data. *J Geophys Res Space Phys* 119:3150–3161. <https://doi.org/10.1002/2013JA019487>
- Yamazaki Y, Matthias V, Miyoshi Y, Stolle C, Siddiqui T, Kervalishvili G, Alken P (2020) September 2019 antarctic sudden stratospheric warming: Quasi-6-day wave burst and ionospheric effects. *Geophys Res Lett* 47(1):e2019GL086577. <https://doi.org/10.1029/2019GL086577>

## Publisher's Note

Springer Nature remains neutral with regard to jurisdictional claims in published maps and institutional affiliations.